The Journal of Chemical Physics

RESEARCH ARTICLE | MARCH 26 2024

Revisiting the benzene excimer using [2,2] paracyclophane model system: Experiment and theory **⑤**⊘

Omer Haggag ⁽ⁱ⁾; Roi Baer ⁽ⁱ⁾; Sanford Ruhman ⁽ⁱ⁾; Anna I. Krylov ⁽ⁱ⁾

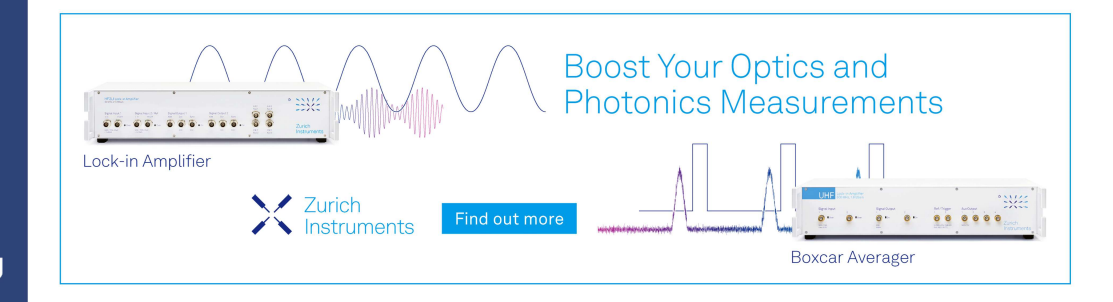


J. Chem. Phys. 160, 124111 (2024) https://doi.org/10.1063/5.0196641





20 Midi CIT 2024 21.00





Revisiting the benzene excimer using [2,2] paracyclophane model system: Experiment and theory 0

Cite as: J. Chem. Phys. 160, 124111 (2024); doi: 10.1063/5.0196641 Submitted: 8 January 2024 • Accepted: 6 March 2024 • Published Online: 26 March 2024













Omer Haggag, De Roi Baer, De Sanford Ruhman, De and Anna I. Krylov De III (1975)







- ¹ Institute of Chemistry, The Hebrew University of Jerusalem, Givat Ram, Jerusalem 9190401, Israel
- ²Fritz Haber Center for Molecular Dynamics, Institute of Chemistry, The Hebrew University of Jerusalem, Givat Ram, Jerusalem 9190401, Israel

ABSTRACT

We report high-level calculations of the excited states of [2,2]-paracyclophane (PCP), which was recently investigated experimentally by ultrafast pump-probe experiments on oriented single crystals [Haggag et al., ChemPhotoChem 6 e202200181 (2022)]. PCP, in which the orientation of the two benzene rings and their range of motion are constrained, serves as a model for studying benzene excimer formation. The character of the excimer state and the state responsible for the brightest transition are similar to those of the benzene dimer. The constrained structure of PCP allows one to focus on the most important degree of freedom, the inter-ring distance. The calculations explain the main features of the transient absorption spectral evolution. This brightest transition of the excimer is polarized along the inter-fragment axis. The absorption of the light polarized in the plane of the rings reveals the presence of other absorbing states of Rydberg character, with much weaker intensities. We also report new transient absorption data obtained by a broadband 8 fs pump, which time-resolve strong modulations of the excimer absorption. The combination of theory and experiment provides a detailed picture of the evolution of the electronic structure of the PCP excimer in the course of a single molecular vibration.

Published under an exclusive license by AIP Publishing. https://doi.org/10.1063/5.0196641

I. INTRODUCTION

Excimers and exciplexes are important players in many photochemical processes. They are complexes of two molecular fragments that interact weakly in the ground electronic state but form much stronger bonds upon electronic excitation. Excimers are formed by two identical fragments, whereas exciplexes are formed by two different fragments.

The driving force for excimer formation is explained by the molecular orbital theory, as illustrated in Fig. 1 for the helium dimer. In the ground electronic state, interaction between the two He atoms is very weak because the formal bond order is zero. However, upon electronic excitation (or ionization), the bond order increases, giving rise to a strongly bound dimer. To highlight the similarity with the quantum-mechanical picture of covalent bonding, we refer to this description as the DMO-LCFMO (dimer molecular orbitals-linear

combination of fragment molecular orbitals) framework. DMO-LCFMO explains trends in the ionization energies of π -stacked nucleic acid bases and other aromatic dimers¹⁻³ as well as excimer formation in liquid helium4,5 and benzene.6

Excimers were first observed in mercury⁸ and helium^{9,10} dimers. The first observation of aromatic excimers (formed by pyrene) was reported in 1954 by Förster and Kasper. 11 As a prototypical aromatic molecule, benzene has been the subject of numerous experimental and theoretical studies. The formation of excimers in benzene was first observed experimentally by Birks in 1968. 12,13 It manifests in a strong and broad absorption band at 2.4-2.5 eV, located below the benzene monomer's lowest excited singlet state. The nature of the transition has been somewhat unclear—because of symmetry considerations, Birks' initial assignment of this transition to $B_{1g} \rightarrow E_{1u}$ was questioned. Later, theoretical analyses and highlevel calculations confirmed⁶ that the strong excimer absorption

Department of Chemistry, University of Southern California, Los Angeles, California 90089, USA

^{a)}Authors to whom correspondence should be addressed: sandy@mail.huji.ac.il and krylov@usc.edu

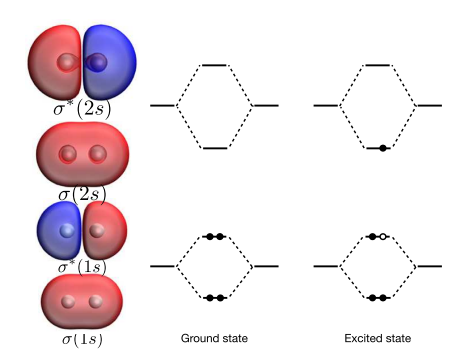


FIG. 1. Molecular orbital diagram explaining excimer formation in He $_2$. In the ground electronic state, $\sigma(1s)^2\sigma^*(1s)^2$, the formal bond order is zero, giving rise to a very shallow potential energy curve (bonding energy of 11 K). However, upon electron promotion from $\sigma^*(1s)$ to $\sigma(2s)$, the bond order becomes one, resulting in the formation of strongly bound He $_2^*$. This diagram also suggests the existence of a bright excimer transition, $\sigma(2s) \to \sigma^*(2s)$, polarized along the He–He axis and resulting in a repulsive electronic state.

can indeed be assigned to this transition—a small distortion lowering symmetry from D_{6h} to D_{2h} splits the optically forbidden E_{1u} state into dark and bright components, with the bright component being polarized along the inter-fragment axis, as expected for the excimer transition. In the DMO-LCFMO framework, this transition is similar to the $\sigma(2s) \rightarrow \sigma^*(2s)$ transition in the helium dimer (Fig. 1). This study also noted a mixed valence–Rydberg character of the bright excimer state and that this state is embedded in a dense manifold of much darker electronic states.

In a previous study, we used ultrafast time-resolved pump-probe spectroscopy to interrogate the dynamics of excimer formation in liquid benzene. We found that the characteristic excimer absorption appears within 50 fs following the excitation and then increases fourfold in the course of 100 ps. While the rearrangement of the benzene molecules to form an excimer structure (tight sandwich) explains the slow rise, the fast appearance was puzzling. The calculations attributed it to the delocalized excitations supported by suitably oriented pairs of molecules, which are present in liquid benzene in sufficient amounts due to its disordered structure and thermal fluctuations. The highly disordered structure of the liquid, the presence of multiple configurations, and significant structural rearrangements involved in the formation of the excimer complicate the interpretation of time-resolved spectroscopic data.

These issues have motivated us to revisit the electronic states of benzene dimer and excimer formation using a model system in which benzene moieties are constrained to the sandwich configuration by covalent bridges. Here, [2,2]-paracyclophane (PCP) is such a model system (see Fig. 2). In addition to the constrained molecular structure, the crystal packing of PCP allows one to distinguish between the absorption components polarized along and perpendicular to the rings plane. $^{15-17}$ Figure 3 shows the crystal structure of PCP. The unit cell of this tetragonal crystal contains two molecules of PCP. The benzene rings of the molecules are perpendicular to each other, and their long axes (the x axes) are parallel and coincide with the crystal's unique direction (c). Accordingly, light propagating perpendicularly to the crystal plane measures the

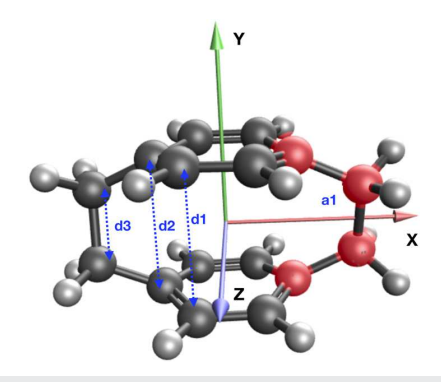


FIG. 2. PCP structure, definitions of the axes, key distances $(d_1 - d_3)$, and dihedral angle a_1 defined by highlighted atoms.

absorption component along the x axis (in-plane) if its polarization is set to coincide with this direction. Setting the light polarization perpendicular to the x axis measures the combined absorption along the y (inter-ring) and z (in-plane short axis) axes. These polarization measurements afford a more detailed understanding of excimer's optical properties.

Recently, some of us reported the results of time-resolved experiments on PCP single crystals. ¹⁸ The two benzene rings in PCP are already parallel, and the excitation induces structural relaxation along the inter-ring coordinate, leading to a large-amplitude breathing motion. The polarization data suggested that several absorbing states contribute to the signal and revealed absorbing components

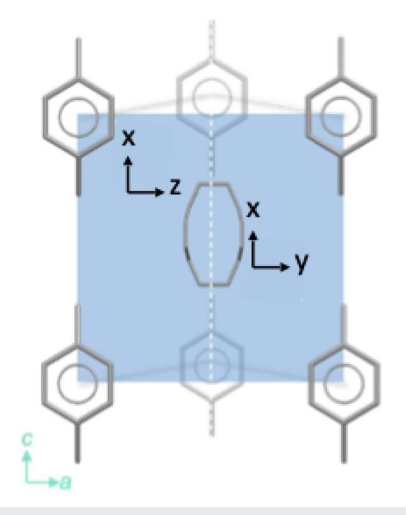


FIG. 3. Crystal structure of PCP. a-c is the crystal plane. Black axes show the internal coordinate frames (see Fig. 2) of the two molecular orientations present in the unit cell. Light polarized along the a direction probes transitions along the y and z axes, and light polarized along the c direction probes transitions along the x axis

polarized along all three molecular axes, with the inter-ring component (y+z) nearly twice as intense as the in-plane component (x). However, the nature of the absorbing states was not characterized.

Here, we present a detailed theoretical analysis of the excimer formation in PCP and its absorption using state-of-the-art quantum chemical calculations. As in our previous studies, 6,7 we employ the equation-of-motion coupled-cluster method for excitation energies with single and double substitutions (EOM-EE-CCSD or EOM-CCSD for short), ^{19,20} which is capable of describing states of mixed character (here, valence and Rydberg²¹). In contrast to the previous studies, we use a larger basis set with additional sets of diffuse functions, 6-311(2+,+)G(d,p).

We also present new experimental results. Our previous study¹⁸ has shown that excimer absorption polarized along the inter-ring axis features several bands with intensities that are strongly dependent on the inter-ring distance. Using the narrow bandwidth UV pump (FWHM = 4 nm), 18 we were able to resolve the vibrational period of the inter-ring breathing mode but were not able to achieve sub-period resolution because the excitation pulse duration was insufficient for achieving perfect localization of the reactive wavepacket in the excited state. Here, we use a broadband UV pump (FWHM = 30 nm), which significantly improves the localization of the wave-packet, affording precise mapping of the energy differences between the PESs in the course of a vibrational period (more on this in Sec. III). This mapping enables a quantitative comparison between theory and experiment.

Figure 2 shows the structure of PCP in the standard Q-Chem orientation,²² along with the definitions of the key structural parameters. The calculations show that the system has a D_2 symmetry both in the ground state and in the lowest excited state (excimer state). In a perfect sandwich configuration, the symmetry is D_{2h} . The deviation from D_{2h} can be explained by the structural strain, which results in slight twisting of the benzene rings (shown in Fig. S1 in the supplementary material). The strain is also responsible for the warping of the benzene rings. The distances d_1 and d_2 represent the distance between the two benzene moieties. In a perfect sandwich

arrangement, $d_1 = d_2$; however, the structure of PCP is strained and benzene rings are puckered. The difference between d_1 and d_2 can characterize the extent of the deformation. Another important parameter is the dihedral angle a_1 . In a perfect sandwich configuration of D_{2h} symmetry, this dihedral angle is zero; hence, the value of a_1 quantifies the deviation from D_{2h} . In the excited state, the excimer formation results in a shorter distance between the rings, as discussed in detail below. This inter-ring breathing motion, activated by electronic excitation, modulates excimer absorption. Quantitative understanding of these modulations is the main focus of this

In our pump-probe experiment, we excite the PCP crystal (Fig. 3) with a broadband pump centered around 300 nm (4.13 eV) polarized along x, and then monitor the excited-state dynamics using ultrafast probe pulses in the range of 400-750 nm (3.10-1.65 eV). The pump is always aligned along the x axis using birefringent properties of PCP crystals. We then control polarization of the probe relative to the pump and measure the transient absorption polarized along x (in-plane long axis) and along y + z (inter-ring and in-plane short axis). A detailed description of the experimental setup is given below.

II. COMPUTATIONAL DETAILS

All calculations were done with the Q-Chem quantum chemistry program.^{23,24} We use Q-Chem's symmetry convention²² throughout the manuscript, meaning that the b_1 and b_2 irreps are flipped relative to the standard Mulliken convention (see Table S1 in the supplementary material).

We optimized the ground-state (S₀) structure of PCP (shown in Fig. 2 and in Fig. S1 in the supplementary material) using two range-separated functionals augmented with dispersion correction, ω B97X-D and CAMB3LYP-D. The excimer structure was obtained by optimizing the lowest excited state (1¹B₂, S₁). EOM-CCSD, ωB97X-D, and CAMB3LYP-D were used for the excited-state geometry optimization. In CAMB3LYP-D calculations, D3_ZERO dispersion correction was used (both in the ground and excited

TABLE I. Essential structural parameters of PCP in the ground and first excited states. Figure 2 shows the definition of structural parameters; ω_{br} and ω_{tw} are frequencies of the breathing and twisting modes, respectively.

State/method ^a	d1 (Å)	d ₂ (Å)	d ₃ (Å)	<i>a</i> ₁ (°)	$\omega_{br} (\mathrm{cm}^{-1})$	$\omega_{tw} (\text{cm}^{-1})$
S ₀ /exp ^b	3.099	2.784	1.593	-12.83	241	72
$S_0/\omega B97X-D$	3.115	2.800	1.591	-18.12	256.5	78.8
S ₀ /CAMB3LYP-D	3.106	2.796	1.593	-14.80	251.0	60.5
S ₁ /exp ^c					233	72 ^d
$S_1/\omega B97X-D$	2.903	2.617	1.571	-13.6		
S ₁ /CAMB3LYP-D	2.903	2.622	1.571	-11.0	249.3	29.2
S ₁ /EOM-CCSD	2.931	2.630	1.577	-13.6	233.4 ^e	

^aAll optimization and frequency calculations were performed with the 6-311+G(d,f) basis.

^bFrom Refs. 35-37, the experimental dihedral and bond lengths were taken at 15 K (Ref. 37). The vibrational frequencies were taken from Refs. 35 and 36

cFrom Ref. 18.

dIn solution.

eNumeric estimate; see the supplementary material.

states). All geometry optimizations and frequency calculations were carried out with the 6-311+G(d,p) basis set. Because we could not resolve the persistent imaginary frequency in calculations using ω B97X-D, we modeled the potential energy surface (PES) scans using CAMB3LYP-D/6-311+G(d,p) structures and normal modes. Both CAMB3LYP-D and EOM-CCSD yield D_2 excimer structures. The essential structural parameters are collected in Table I. The Cartesian geometries of the optimized structures and vibrational frequencies are given in the supplementary material.

The excited states were computed using the EOM-CCSD and CAMB3LYP-D methods with the 6-311(2+,+)G(d,p) basis set. Additional calculations were carried out with aug-cc-pVTZ. To reduce computational costs, we used single precision in EOM-CC calculations.²⁵ Core electrons were frozen in correlated calculations. An example of an input file for these calculations is given in the supplementary material.

We used natural transition orbitals (NTOs) and corresponding exciton descriptors $^{26-30}$ to characterize electronic transitions. In particular, we used hole and particle sizes to quantify the extent of the Rydberg character and the participation ratio (PR_{NTO}) to quantify the essential number of configurations contributing to transitions, similar to our previous work. We note that these descriptors can also help distinguish between excimers and excitons, as was shown by Plasser and Lischka. This analysis was carried out using the *libwfa* package.

To identify Franck–Condon active modes, we used the ezFCF program.³⁴ We then generated displacements along the Franck–Condon active mode and used them to compute excimer's absorption spectra at different geometries. The computed stick spectra were convoluted with Gaussians (σ = 0.1 eV).

To model transient absorption spectra, we mapped the structures to the probe times using the classic harmonic oscillator model; more details are given below.

III. EXPERIMENTAL DETAILS

A. Sample preparation

Thin single crystalline PCP samples were prepared by melting several grains (97% grade, Sigma-Aldrich, with no further purification) in between 160 $\mu \rm m$ thick quartz cover slips, followed by rapid cooling to room temperature. Single crystal areas of ~25 mm² were then characterized and oriented by conoscopic microscopy. Further information on the crystallization and characterization processes can be found elsewhere. 18 The sample was mounted on a rotating holder, used for alignment of the long-axis direction (x axis, see Figs. 2 and 3) with the pump polarization. To avoid the gradual degradation observed when irradiating static specimens, the holder was mounted on a 2D motorized stage (Newmark systems), set to move continuously in the plane perpendicular to the direction of probe propagation.

B. Ultrafast spectroscopy

Figure 4 shows the experimental setup. The femtosecond pump-probe measurements were performed with a home-built amplified Ti:sapphire laser system producing 1 kHz of 1 mJ 30 fs pulses centered at 800 nm.

A broadband UV pump centered at 300 nm (FWHM = 30 nm) with a duration of ~8 fs was generated by sum frequency generation (SFG). Broadband visible pulses centered at 540 nm (FWHM = 100 nm) were generated by a single pass of a fraction of the 800 nm seed through a noncollinear OPA (NOPA) and then compressed by a series of reflections onto a pair of dielectric double-chirped mirrors. These pulses were then mixed with narrow-band pulses centered at 690 nm, generated by an OPA (TOPAS 800), followed by doubling on a type I BBO crystal. These two beams were then focused onto a 100 μ m type II BBO crystal to generate the desired UV pump.

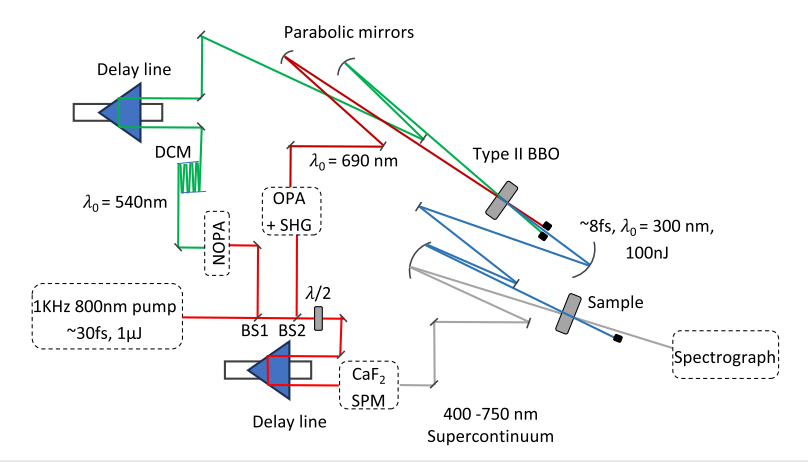


FIG. 4. Ultrafast pump—probe setup for the generation of a compressed broadband UV pump (300 nm) through sum frequency generation and a supercontinuum probe generated by self-phase modulation (SPM) of the 800 nm pump. Notations: BS1 and BS2 are beam splitters with a reflection/transmission ratio of 50:50 and 70:30, respectively; DCM: double-chirped mirror setup; λ/2: half-wave plate; NOPA: non-collinear optical parametric amplification setup; OPA: optical parametric amplification setup; SHG: second harmonic generation; delay line: retro-reflector mounted on a motorized stage with μm resolution.

Supercontinuum probe pulses in the range of 400–750 nm were generated by focusing the 800 nm seed on a 2 mm plate of CaF₂. A $\lambda/2$ wave plate was introduced into the probe path to control polarization of the probe pulse relative to the pump.

To align the pump polarization with the molecular x axis, we used the birefringent properties of the uni-axial PCP crystal. Following full blockage of the pump by a UV polarizer, the crystal sample was introduced into the optical path. Then, the crystal film was rotated to fully darken the pump transmission.

As mentioned in the Introduction, in the present experiments, we improved time resolution using the broadband pump. In the previous study, 18 we used a narrow bandwidth UV pump (FWHM = 4 nm) with a 30 fs duration assuming a transformlimited Gaussian centered at 300 nm, which was sufficient to probe the vibrational period of the inter-ring breathing mode. However, the vibrational wave-packet induced on S1 was too broad. Figure S2 in the supplementary material shows a simulated wavepacket induced on the S1 PES under these conditions. During the period of vibration, the probability density of the wave-packet shifts from side to side, while maintaining a notable density throughout the entire allowed coordinate space. Due to this delocalization of the wave-packet, we could only partially resolve the evolution of the transient absorption within the vibrational period. Figure S3 in the supplementary material shows the simulations corresponding to the current experiment, a broadband UV pump pulse (FWHM = 30 nm) with a duration of ~8 fs. As one can see, the localization of the wave-packet induced on S₁ is significantly improved, allowing us to resolve instantaneous energy gaps between the electronic states of the excimer.

IV. RESULTS AND DISCUSSION

Figure 5 shows the sketch of the present experiment, highlighting the differences between the frequency-domain and time-domain approaches. The excimer state (S_1 state) is characterized by increased

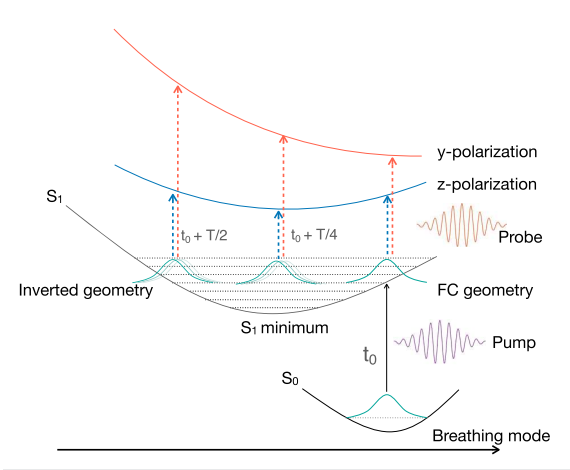


FIG. 5. Sketch of the relevant electronic states and time-resolved mapping of the excimer absorption. Breathing mode corresponds to the inter-ring distance.

bonding interactions between the two benzene rings relative to the ground state. The characteristic strong excimer absorption is dominated by the transition to the repulsive state (red curve), polarized along the inter-fragment axis. Because this state is strongly repulsive, excimer's absorption spectrum is broad and featureless—as expected from the reflection principle. The information about the states responsible for excimer absorption (e.g., if there is more than one state involved) and the exact shape of the corresponding PES is hidden in the frequency-domain spectrum. In contrast, the timeresolved measurements can reveal these details. Briefly, the pump excites the PCP to the S1 state (excimer state), creating a vibrational wave-packet at the Franck-Condon (FC) point. This is an endpoint of the ensuing vibrational motion along the breathing mode. The wave-packet moves toward the S₁ minimum but due to the acquired momentum, overshoots to an inner turning point along the breathing normal mode (inverted geometry, which corresponds to the compressed structure). As the wave-packet evolves on S1, the broadband probe pulses produce spectra corresponding to the specific positions of the wave-packet and reporting on the instantaneous energy gaps between the S1 and absorbing states as well as respective oscillator strengths. The precision of this report depends on the degree of localization of the wave-packet, which is very tight in the present experiment owing to the extreme shortness of the pump. Analysis of the spectral modulations as a function of the probe wavelength and polarization can reveal whether the modulations are due to a coordinate dependence of the vertical energy gaps between the PESs or due to a coordinate dependence of the transition dipole moments (non-Condon effects). Finally, the large frequency range of the probe allows observing the transitions to several absorbing

In the discussion below, we focus on the three structures—Franck–Condon point, the S_1 minimum, and the inner turning point corresponding to the compressed geometry. Polarization measurements allow disentangling contributions from different absorbing states (e.g., blue vs red).

A. Molecular orbital framework and symmetry

The D_2 character table is given in the supplementary material. Using the molecular orientation²² shown in Fig. 2, the z axis belongs to the b_1 irrep, the x axis belongs to the b_2 irrep, and the y axis belongs to the b_3 irrep. Hence, transitions polarized along y+z, which correspond to the inter-ring and short in-pane axes, belong to the b_1 and b_3 irreps, and transitions polarized along x, which corresponds to the in-plane long axis, belong to the b_2 irrep.

The lowest excited state of PCP is B_2 (using the molecular orientation shown in Fig. 2). At the S_0 geometry, this state is located 4.41 eV above the ground state [at the EOM-CCSD/6-311(2+,+)G(d,p) level of theory] and is weakly allowed (f_1 = 0.001, polarized along the x-axis). Figure 6 shows the NTOs for the $S_0 \rightarrow S_1$ transition. They are very similar to the NTOs of the analogous transition in the benzene dimer, 6,7 confirming that PCP is a good model of the benzene dimer. Hole NTOs can be described as anti-bonding (with respect to the two benzene rings) combinations of the π -type HOMOs, and particle NTOs can be described as bonding combination of the π^* -type LUMOs. Thus, similar to the He $_2$ example (Fig. 1), the transition results in bonding interactions between the two rings so that the excitation to S_1 leads to significant

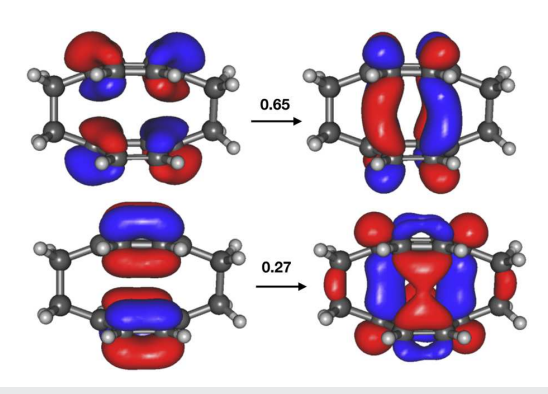


FIG. 6. NTOs for the transition from the ground state to the lowest excited state (1B₂) at the optimized geometry of the excimer; EOM-CCSD/6-311(2+,+)G(d,p). Renormalized squares of singular values. $\Omega=0.78$, $PR_{NTO}=2.0$, particle size = 2.6 Å.

structural relaxation. According to calculations, in the S_1 state, the two benzene rings come closer to each other, lowering the total energy by 0.34 eV. At the S_1 optimized structure, the vertical excitation energy for the $S_0 \rightarrow S_1$ transition is 3.83 eV. We note that $PR_{NTO} = 2.0$ reflects the electronic degeneracy present in the benzene moieties and reveals the absence of contributions of excitonic configurations, ^{14,32} as expected at this structure of the fully formed excimer.

The allowed transitions in the D_2 point group are of B_1 , B_2 , and B_3 symmetries; they are polarized along z, x, and y axes, respectively. Thus, for the excimer state (B_2), the allowed target states are A, B_1 , and B_3 , with the respective transitions polarized along x, y, and z, respectively. With our setup, we can measure transient absorption for transitions polarized along x and along y+z axes. Detailed analysis of the excited states of the PCP excimer is given below.

B. Structures of PCP in the \mathbf{S}_0 and \mathbf{S}_1 states and Franck-Condon factors

As Table I shows, the short ethane bridges ($d_3 = 1.59 \text{ Å}$) make the inter-ring distance shorter than the distance between the rings in a parallel-displaced structure of the benzene dimer (3.60 Å), ³⁸ which results in a warping of the benzene rings and an outward displacement of the non-tethered carbons, i.e., $d_1 - d_2 = 0.32 \text{ Å}$. The computed bond lengths and dihedral angle agree with the experimental values obtained by the XRD measurements on single crystals of PCP.³⁷ Normal-mode analysis of the optimized S₀ structure yields an inter-ring breathing mode of 251 cm⁻¹, in line with the experimental values measured by Raman and emission spectroscopy. ^{35,36}

As anticipated from the molecular orbital analysis, the $S_0 \rightarrow S_1$ excitation leads to a shortening of the inter-ring distance (by ~0.2 Å), accompanied by the reduction in the dihedral angle; the d_2-d_1 difference is also reduced. The value of $d_1=2.903$ Å is shorter than the computed equilibrium distance (3.1–3.2 Å) between the rings in the benzene excimer, 6 which means that the excimer structure of PCP is also strained relative to the benzene excimer.

The S_1 vibrational analysis yields an inter-ring breathing frequency of 249 cm⁻¹ and twisting frequency of 29 cm⁻¹, in-line with the experimental values obtained from the excitation spectrum of cold PCP crystals^{15,16} and transient absorption data of the PCP excitations are consistent as the property of the

Within the double-harmonic parallel-mode approximation (a displaced harmonic oscillator model), ezFCF calculation³⁴ shows that the most active Frank–Condon mode for the $S_0 \rightarrow S_1$ excitation corresponds to the inter-ring breathing vibration with a 1.1772 Å \sqrt{amu} displacement (calculated using the normal modes of the S_1 state). We also computed the Huang–Rhys factors (i.e., the number of vibrational levels for a given mode accessible upon vertical transition) for this transition using the following equation:

$$s_k = \frac{1}{2} \cdot \left(\frac{\omega_k \cdot \|\Delta \tilde{q}_k\|^2}{\hbar} - 1 \right), \tag{1}$$

where s_k , ω_k , and $\|\Delta \tilde{q}_k\|$ denote the Huang–Rhys factor, frequency, and mass-weighted displacement along the kth normal mode, respectively. Given the ground-state (\vec{r}_0) and excited-state (\vec{r}_1) Cartesian geometries, the mass-weighted displacement along the kth normal mode is calculated according to the following equation:

$$\|\Delta \tilde{q}_k\| = \tilde{q}_k^{\dagger} \cdot M^{\frac{1}{2}} \cdot (\vec{r}_1 - \vec{r}_0),$$
 (2)

where \tilde{q}_k^{\dagger} represents the kth mass-weighted normal mode and $M^{\frac{1}{2}}$ is a diagonal matrix containing the square-roots of masses ordered according to their positions in the displacement vectors. The computed Huang–Rhys factors yield s=5 for the inter-ring breathing mode (see Fig. S4 in the supplementary material) and $s\approx 0$ for the rest

Accordingly, we generated 21 Cartesian geometries, $\vec{R}(n)$, for displacements along the breathing mode centered around the S₁ minimum (zero displacement, n = 0),

$$\vec{R}(n) = \vec{r}_1 \pm \frac{n}{10} \cdot \|\Delta \vec{r}_{br}\| \cdot \vec{r}_{br} \quad n = 0, 1, \dots, 10,$$
 (3)

where \vec{r}_{br} represents the breathing mode and $\|\Delta \vec{r}_{br}\|$ represents the total displacement along this mode, both in the Cartesian units (Å),

$$\|\Delta \vec{r}_{br}\| = \vec{r}_{br}^{\dagger} \cdot (\vec{r}_1 - \vec{r}_0). \tag{4}$$

The displacements range from -0.474 to 0.474 Å in Cartesian coordinates and from -1.2 to 1.2 Å \sqrt{amu} in mass-weighted coordinates, with 0.474 corresponding to the Franck–Condon point, zero corresponding to the the S₁ minimum, and -0.474 corresponding to the inner turning point of the breathing mode (the most compressed structure).

To validate the displacements and to estimate anharmonicity, we numerically solved the vibrational problem using the computed PES scans (see Fig. S4 in the supplementary material). The numerically computed harmonic frequencies are very close to the analytic CAMB3LYP-D value for the CAMB3LYP-D curve (249.9 vs 249.3 cm⁻¹), whereas the EOM-CCSD curve yielded a smaller value (233.4 cm⁻¹). The anharmonicities for both curves were negligible. We note that the EOM-CCSD frequency of the breathing mode of the excimer is in remarkably good agreement with the experimental value.

C. Excited states of PCP

Figure 7 shows excited-state PESs along the inter-ring breathing mode computed with EOM-CCSD/6-311(2+,+)G(d,p) (the CAMB3LYP-D results are shown in the supplementary material). The lowest state is the excimer state (1B₂). We computed 12 excited states of A symmetry, 17 excited states of B₁ symmetry, one excited state of B2 symmetry (excimer state), and 12 excited states of B3 symmetry. At zero displacement (excimer structure), this covers energy ranges up to 7.09, 7.00, and 7.13 eV in the A, B₁, and B₃ symmetries relative to the ground state or, equivalently, up to 3.19, 3.10, and 3.23 eV relative to the excimer state (located at 3.90 eV). As one can see, the manifold of electronic states is very dense. Hence, it is not surprising that the transient absorption cannot be modeled by assuming a single absorbing state with fixed oscillator strength. According to the NTO analysis, the states can be described as valence-like and Rydberg-like excitations, as well as states of mixed character.²¹ Importantly, different states show different dependences on the inter-ring distance, which can be rationalized by the shape of the corresponding NTOs. In the discussion below, we focus our analysis on the states relevant to excimer absorption.

To recall the transient-absorption setup and the definitions of the relevant structures, we refer readers to Fig. 5. After the discussion of the computed PESs, one can now appreciate the additional complexity of PCP in which multiple electronic states are contributing to the excimer absorption.

Figure 8 shows the computed excimer absorption spectrum at zero displacement (i.e., at the S_1 minimum). The brightest peak in the excimer absorption spectrum corresponds to the $1B_2 \rightarrow 9B_1$ transition at 2.4 eV ($f_I=0.1237$, polarized along y). NTOs for the $S_0 \rightarrow 9B_1$ transition are shown in Fig. S6 in the supplementary material. Based on the orbital shapes and exciton descriptors, this state has mixed valence/Rydberg character—compare the particle sizes of the $S_0 \rightarrow S_1$ and $S_0 \rightarrow 9B_1$ transitions (2.6 vs 3.7 Å). Figure 9 shows NTOs for the $1B_2 \rightarrow 9B_1$ transition, which visualizes the changes in electron density for the excimer absorption. The valence NTOs for the $1B_2 \rightarrow 9B_1$ transition correspond to the transition from bonding to anti-bonding (with respect to the fragments)

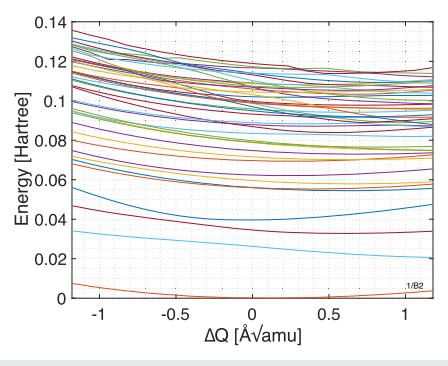


FIG. 7. Excited-state potential energy surfaces of PCP along the inter-ring breathing mode; EOM-CCSD/6-311(2+,+)G(d,p). The lowest state is 1B₂, the rest of the states are of A, B₁, and B₃ symmetries; higher B₂ states are not shown.

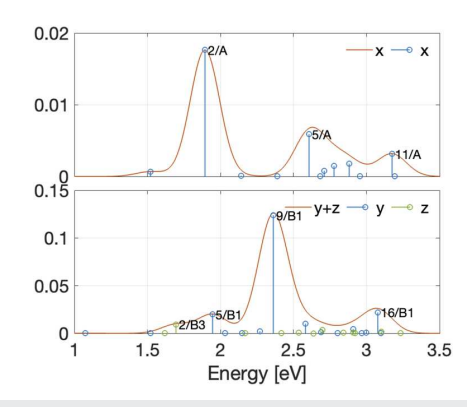


FIG. 8. Excimer absorption spectra at the excimer geometry $(S_1 \text{ minimum})$ for two polarizations (x and y + z); EOM-CCSD/6-311(2+,+)G(d,p).

orbitals, leading to the strongly repulsive PES. This orbital picture is similar to the bright excimer state characterized in Ref. 6, but with a larger Rydberg contribution, in part, because here we use a larger basis with more diffuse functions. The computed transition energy (2.36 eV) is lower than the computed transition energy in the benzene excimer reported in Ref. 6 (3.04 eV). Larger contributions of Rydberg configurations in PCP explain the lower oscillator strength of the transition (0.12 here vs 0.3 in Ref. 6). The next bright state in the z + y polarization is $16B_1$ at about 3.1 eV ($f_1 = 0.0220$), i.e., 0.7 eV above $9B_1$. The rest of the states have very low oscillator strengths.

For the transitions polarized along x (A states), the brightest one is the 2A state at 1.89 eV ($f_l = 0.0176$). Its oscillator strength is 6.8 times smaller than that of the 9B₁ state. The next brightest state is 5A at 2.61 eV ($f_l = 0.0059$). NTOs for these two transitions are shown in Fig. 10. The particle sizes for these transitions are 6.2 and 7.0 Å, respectively, revealing their predominantly Rydberg character.

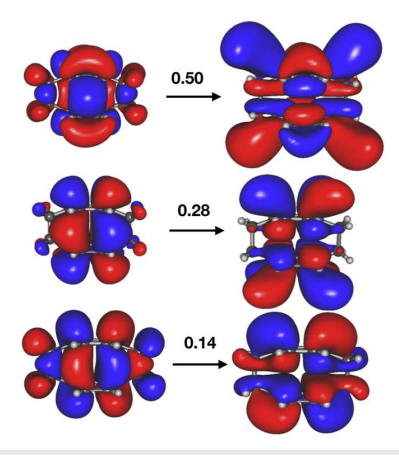


FIG. 9. NTOs for the transition $1B_2 \to 9B_1$ (brightest transition in excimer absorption) at the optimized geometry of the excimer. EOM-CCSD/6-311(2+,+)G(d,p). Renormalized squares of singular values. $\Omega=0.26,\ PR_{NTO}=2.8,\ particle$ size = 3.2 Å.

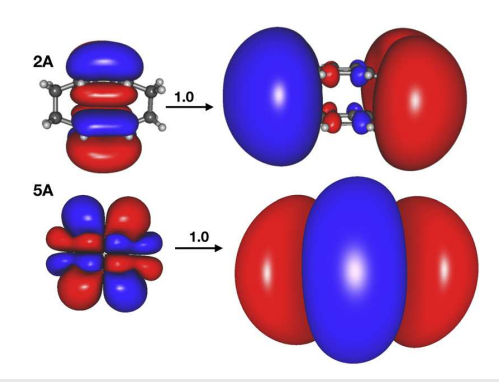


FIG. 10. NTOs for the transition from the ground state to the 2A and 5A states (the brightest transitions in excimer absorption for polarization along the x axis) at the optimized geometry of the excimer. EOM-CCSD/6-311(2+,+)G(d,p). Renormalized squares of singular values. 2A state: $\Omega = 0.83$, $PR_{NTO} = 1.0$, particle size = 6.2 Å. 5A state: $\Omega = 0.84$, $PR_{NTO} = 1.02$, particle size = 7.0 Å.

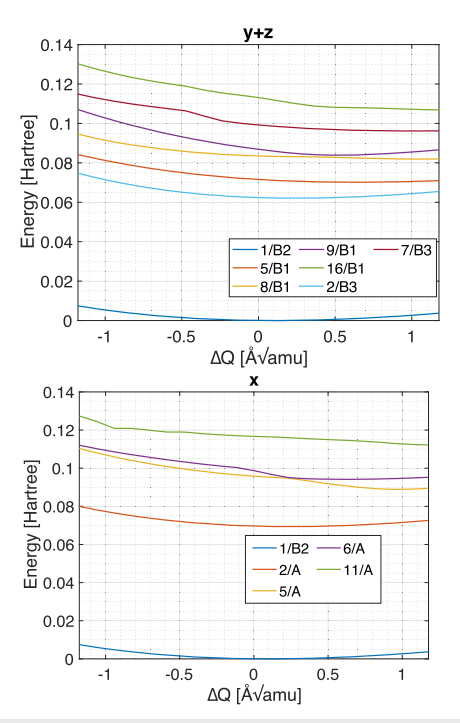


FIG. 11. Excited-state potential energy surfaces of PCP along the inter-ring breathing mode for the excimer state and the brightest transitions in each polarization; EOM-CCSD/6-311(2+,+)G(d,p). Zero displacement corresponds to the S₁ minimum, FC point is on the right, and the compressed geometry (inner turning point, inverted structure) is on the left.

Figure 11 shows the PESs corresponding to the brightest transitions in each polarization. As anticipated, the energy of the brightest B₁ state (purple-then-orange curve) strongly depends on the interring distance. We also observe interaction of this bright state with another state from the B₁ manifold, leading to the diabatic-like interchange of the orange and purple curves shown in Fig. 11, which indicates the changes in the character due to the varying weights of valence and Rydberg excitations. This change in the character of the states leads to change in the respective oscillator strengths of the two adiabatic states (orange and purple), as illustrated in Fig. S7 in the supplementary material. From these plots, one can anticipate large variations in the transient absorption polarized along the z + y, with the most blue-shifted absorption corresponding to the inner turning point (compressed geometry)—the difference in the excitation energy of the brightest B1 state at the two turning points is 0.6 eV. The PES of the bright A states are flat (i.e., the difference in the excitation energy of the brightest A state at the two turning points is 0.1 eV), consistent with their Rydberg character. Hence, one can anticipate much smaller spectral modulations in the x-polarized transient absorption in the course of excited-state vibrations. We note that A states also show significant non-Condon effects (Fig. 11, bottom panel, and S7, right panel).

To illustrate variations of the absorption along the breathing mode, we compare the computed spectra at the excimer geometry and the two turning points—the Franck–Condon geometry and the inverted (compressed) structure (see Fig. 5). Figure 12 shows the three spectra for y+z polarization. As expected from the molecular orbital considerations (recall that this transition corresponds to the excitation from a bonding to an anti-bonding orbital), the most intense peak is red-shifted at the FC point relative to the excimer geometry. In addition, the second most intense peak gains intensity at FC geometry so the difference between the two most intense peaks becomes smaller. Passing the S_1 minimum, as the rings come closer, the intensity and energy of the main peak continue to increase and a new peak appears (due to the $12B_1$ state).

The spectra for *x* polarization are shown in Fig. 13. The difference between the three spectra is much smaller, again, in agreement

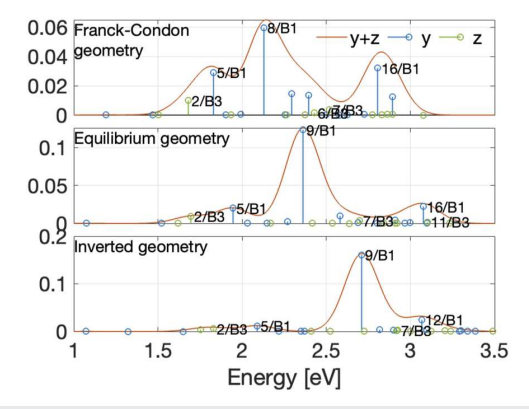


FIG. 12. Excimer spectrum polarized along y+z for transitions at the FC geometry (top), S_1 minimum (middle), and inverted (compressed) geometry (bottom) (with $\sigma=0.1$ eV Gaussian broadening).

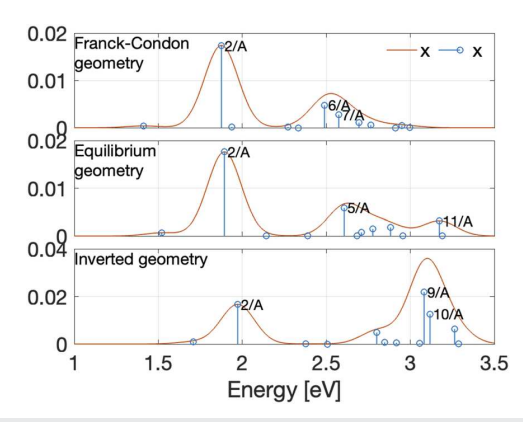


FIG. 13. Excimer spectrum polarized along x for transitions at the FC geometry (top), S_1 minimum (middle), and inverted (compressed) geometry (bottom) (with $\sigma = 0.1$ eV Gaussian broadening).

with the molecular orbital considerations. The most notable change is the increase in the intensity of the secondary peak at the two turning points.

D. DFT vs EOM-CCSD

Figures S8-S10 in the supplementary material show the PESs computed with CAMB3LYP-D. They also show the high density of excited states and capture different slopes of the valence and Rydberg states; however, closer comparison with the EOM-CCSD PES reveals important differences. The differences can be attributed to the residual self-interaction error (SIE), which affects the description of both Rydberg and charge-resonance valence states. For example, the state interaction of the bright B1 states is not captured. Consequently, the computed spectra are notably different, as illustrated in Figs. S10 and S11 in the supplementary material. CAMB3LYP-D correctly identifies the brightest transition for excimer's absorption as a B₁ state with a valence character similar to that of EOM-CCSD; however, its position is strongly red-shifted and its intensity is overestimated compared to that of EOM-CCSD. In the A manifold, the intensity pattern also differs between CAMB3LYP-D and EOM-CCSD. Hence, although the CAMB3LYP-D excimer structures and frequencies agree reasonably well with EOM-CCSD, the excited-states characters and their energies are not accurate. Given its complicated electronic spectrum, PCP can serve as a challenging benchmark for the functional development of excited states.

E. Transient absorption spectra: Theory vs experiment

To connect theory and experiment, we use the computed excitation energies and oscillator strengths at different displacements along the breathing mode to compute the excimer absorption spectra and then compare them with the experimental absorption at the corresponding time delays (see Fig. 5).

We map the structures to the times as follows: Figure 14 shows a transient absorption time trace at the probe energy of 2.2 eV, polarized along y + z. Periodic modulation, which persists throughout the entire probing range, is due to the motion of the wave-packet on the S_1 PES. Fourier transform and decay analysis of the modulating

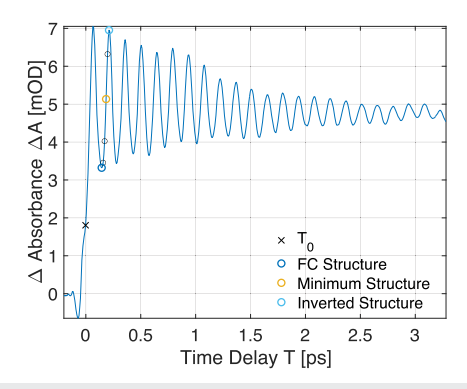


FIG. 14. Representative time trace of the experimental transient absorption for the probe energy of 2.0 eV. The time trace shows periodic modulations at the frequency of the inter-ring breathing mode (233 cm⁻¹) and an exponential decay of 1.2 ps.

residual yields a single frequency of $\omega=233~{\rm cm}^{-1}$ (vibrational period $T_{vib}=144~{\rm fs}$) and an exponential decay lifetime of 1.2 ps. On the basis of the computed Huang–Rhys factors and excited-state frequency calculations, we assign this modulation to the inter-ring breathing mode. Hence, time traces of the transient absorption can be mapped to specific displacements along this coordinate using the classical harmonic oscillator model. For example, the FC structure corresponds to $t=144~{\rm fs}~(T_{vib})$, the inverted (compressed) structure to 211 fs (1.5 T_{vib}), and the S₁ structure corresponds to 180 fs (1.25 T_{vib}).

The theoretical spectra were generated as follows: the stick spectra for the two polarizations at each geometry were convoluted with Gaussians (σ = 0.1 eV) to account for natural broadening. These spectra can be compared with the experimental transient absorption at particular times using the mapping above, this is shown in Figs. 15 and 16. To generate two-dimensional transient absorption spectra, the simulated spectra were convoluted in the time domain with an instrument response function to account for the finite time duration of the pump (Gaussian with a FWHM of 8 fs). Finally, the modulating residual obtained from the simulated transient absorption was multiplied by a decaying exponential function to account for the 1.2 ps lifetime of the breathing vibrations. These spectra are shown in Fig. 18.

The comparison with the experiment requires care because (i) the theoretical calculations are expected to have errors in the absolute values of excitation energies and (ii) experimental spectrum is measured in the 1.75–3.25 eV window. Figures 15 and 16 compare theoretical spectra at the three geometries with the respective experimental traces of the transient absorption. The three theoretical spectra for y+z polarization are red-shifted by 0.57 eV to match the position of the highest peak at the excimer geometry. The theoretical spectra for x polarization are blue-shifted by 0.28 eV to match the position of the highest peak at the excimer geometry. As one can see, once these shifts are applied, the theory and experiment agree reasonably well. The directions of the shifts are consistent with the character of the states—the valence-like $\pi \to \pi^*$ transitions, such as the bright excimer state, are known to be sensitive to dynamic

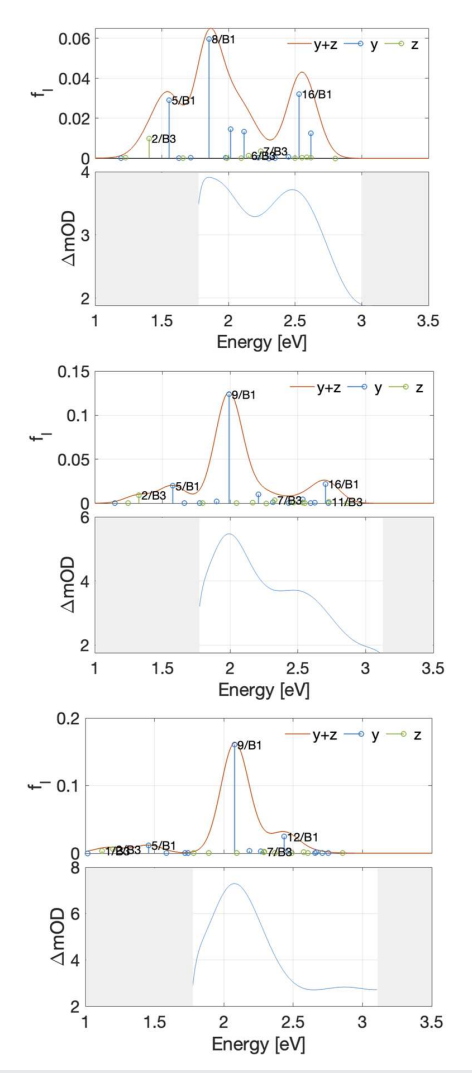


FIG. 15. Theory vs experiment: the excimer spectrum for transitions at the FC (top), S_1 minimum (middle), and inverted (bottom) structures for y+z polarization. In each panel, the computed spectrum is shown on top and the experimental spectrum at the bottom. The theoretical spectrum is red-shifted by 0.57 eV to match the positions of the most intense peaks.

correlation. As a result, EOM-CCSD often overestimates their excitation energies. Hence, the Rydberg states, which are less sensitive to dynamic correlation, appear red-shifted relative to the excimer state.

We note that the ratio of the intensities of the dominant peaks in each polarization is 7:1 in the computed spectra and 3:1 in the experimental transient absorption (at the S_1 minimum). This discrepancy could be due to insufficient correlation treatment; however, it can also be explained by the differences in the radiative lifetimes of the respective states. In the simulations, we applied

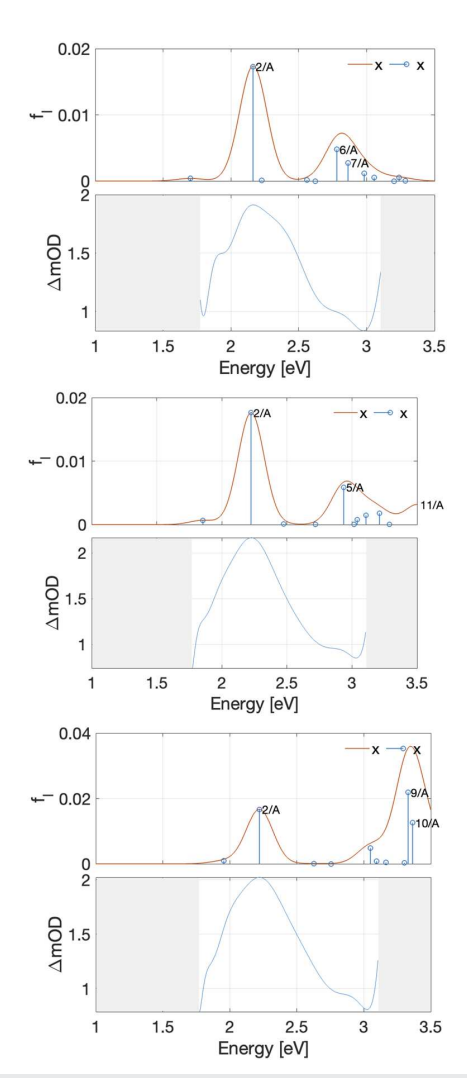


FIG. 16. Theory vs experiment: the excimer spectrum for transitions at the FC (top), S_1 minimum (middle), and inverted structures (bottom) for x polarization. In each panel, the computed spectrum is shown on top and the experimental spectrum at the bottom. The calculated spectrum is blue-shifted by 0.28 eV to match the positions of the most intense peaks.

uniform broadening for all states; however, a simple estimate (see the supplementary material) shows that the radiative lifetime of the $9B_1$ state is 4-5 times shorter than the radiative lifetime of the 2A state. Applying broader Gaussians to the former would reduce the apparent intensities of the computed y + z spectra, bringing the ratio closer to the experimental value.

Finally, Fig. 17 compares the time evolution of the excimer absorption for the two polarizations. As one can see, the trends are reproduced very well, both in terms of energy and intensity changes,

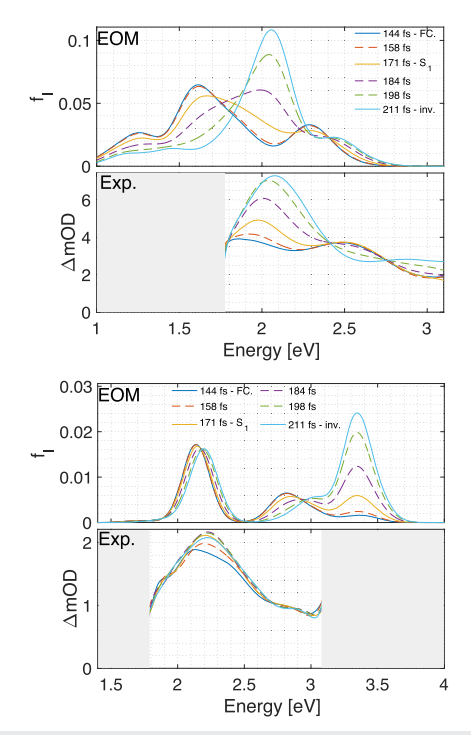


FIG. 17. Simulated and experimental transient absorption spectra. Top: y + z polarization; theoretical spectra red-shifted by 0.57 eV. Bottom: x polarization; theoretical spectra blue-shifted by 0.28 eV. In each panel, the computed spectrum is shown on top and the experimental spectrum at the bottom.

as well as appearance of isosbestic points. These large variations of absorption for the y + z polarization reflect changes in the transition energies and in the character of the absorbing states (e.g., relative weight of Rydberg vs valence contributions) along the breathing

coordinate, as anticipated from the molecular orbital picture and the scans of the PES and transition dipoles. The blue shift (relative to the FC point) of the main peak results from the combination of the Condon and non-Condon effects: as the vibrational wave-packet moves from the FC geometry toward the compressed structure, the $S_1 \rightarrow 9B_1$ energy gap increases by 0.2 eV, and the oscillator strength increases as well at the expense of the $S_1 \rightarrow 8B_1$ transition (see Fig. 11 and Fig. S7 in the supplementary material). The isosbestic points at 2.4 and 2.7 eV reflect the enhancement of the $S_1 \rightarrow 12B_1$ transition at the expense of the $S_1 \rightarrow 16B_1$ transition. Much smaller variations for the x polarization reflect flatter PES of the absorbing Rydberg states. We note that such levels of detail would not be possible to obtain from the frequency-domain measurements.

Figure 18 shows two-dimensional transient absorption maps for both polarizations. Here, we again see strong oscillations for the y+z component and more shallow dynamics for the x component (note the different scales used in the two panels). The higher-energy feature in x component is not accessible in the present experiment. The oscillations persist for several picoseconds, which is quite remarkable for a system with so many degrees of freedom. Such a long coherent motion is possible due to a constrained structure of PCP, which results in a perfectly harmonic potential of a single Franck–Condon active mode.

V. CONCLUSIONS

We presented new time-resolved pump-probe measurements and high-level quantum chemistry simulations of the time-dependent absorption of PCP. The electronic states of PCP are similar to the states of the benzene dimer, both in terms of state energies and molecular orbitals involved in the transitions. Hence, PCP represents a suitable and relevant model of the benzene excimer. With the improved resolution, we are able to resolve the changes in the electronic character of the excimer in the course of a single vibrational period. The simulations explain the main experimental findings and the observed trends in the evolution of the main spectral features in terms of the molecular orbital theory. The excimer spectrum in PCP is dominated by the bright transition polarized along

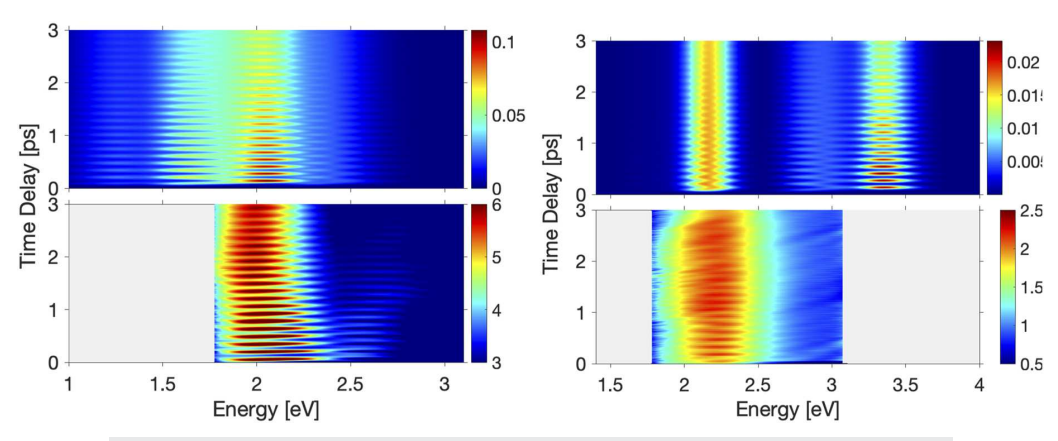


FIG. 18. Experimental and simulated transient absorption maps for the y + z component (left) and the x component (right).

the inter-ring axis. The nature of the excimer state and the bright absorbing state in PCP is very similar to the corresponding states in benzene dimer. The excimer state can be described as the transition from the anti-bonding (with respect to the dimer) orbital formed by benzenes' HOMOs to the bonding (with respect to the dimer) orbital formed by benzenes' LUMOs. The bright absorbing excimer state, polarized along the interfragment axis, can be described as a mixture of valence and Rydberg excitations from the former orbital. Because of this character, the excitation energy for this transition is strongly modulated by the PCP breathing mode. The relative weights of Rydberg vs valence configurations also strongly depend on the structure. In addition to this transition, there are much weaker transitions, predominantly of the Rydberg character, polarized in the plane of the benzene rings. These transitions are dwarfed in the total spectrum but become visible when using a polarized probe.

This work illustrates the power of time-resolved spectroscopy. The strongly repulsive PES of the bright absorbing state and multiple absorbing states exhibiting strong vibronic interactions result in a featureless and not very informative absorption spectrum in the frequency domain. In the time domain, by following the evolution of a narrow vibrational wave-packet on S₁, we were able to follow the PESs of absorbing states along the breathing coordinate and map the experimental spectral evolution into the computed electronic states.

We conclude by emphasizing the importance of the interplay between theory and experiment. Although the present simulations of the transient absorption spectra agree reasonably well with the experiment and explain the main trends, several aspects of the theory call for improvement: (i) improving correlation treatment to achieve quantitative agreement in transition energies (to eliminate the need of empirical shifts), (ii) building theoretical framework to estimate spectral broadening, (iii) extending the capabilities beyond a single Franck–Condon active mode, and (iv) incorporating the quantum nature of the vibrations in the calculation of the spectra.

SUPPLEMENTARY MATERIAL

The supplementary material contains computational details, structures and frequencies, wave-packet simulations, transition dipole moments and state mixing, EOM-CC data, TDDFT PES, and spectra.

ACKNOWLEDGMENTS

This work was supported by the U.S. National Science Foundation (Grant No. CHE-2154482 to A. I. K.) and by the Binational Science Foundation (Grant Nos. 2016102 and 2020105 to S. R.). R. B. acknowledges support from the Israel Science Foundation (ISF 1153/23). O. S. H. was supported by an Azrieli Fellowship awarded by the Azrieli Foundation. We thank Mr. Goran Giudetti (USC) for his help with making orbital images. S. R. and O. S. H. thank Cristian Manzoni for his guidance in setting up the UV-SFG optics. O. S. H. thanks Dr. Hadassah Elgavi Sinai and Dr. Ester Livshits (Fritz Haber Center for Molecular Dynamics, Hebrew University of Jerusalem) for providing information about the BNL functional and its use in TDDFT calculations. Their expertise and support were crucial in the successful completion of this work.

AUTHOR DECLARATIONS

Conflict of Interest

The authors declare the following competing financial interest(s): A. I. K. is the president and a part-owner of Q-Chem, Inc.

Author Contributions

Omer Haggag: Investigation (equal); Visualization (equal); Writing – original draft (equal). Roi Baer: Methodology (equal); Supervision (equal); Writing – review & editing (equal). Sanford Ruhman: Conceptualization (equal); Funding acquisition (equal); Investigation (equal); Methodology (equal); Project administration (equal); Supervision (equal); Writing – review & editing (equal). Anna I. Krylov: Conceptualization (equal); Formal analysis (equal); Investigation (equal); Methodology (equal); Project administration (equal); Supervision (equal); Writing – original draft (equal).

DATA AVAILABILITY

The data that support the findings of this study are available within the article and the associated supplementary material.

REFERENCES

- ¹P. A. Pieniazek, J. VandeVondele, P. Jungwirth, A. I. Krylov, and S. E. Bradforth, "Electronic structure of the water dimer cation," J. Phys. Chem. A **112**, 6159 (2008).
- 2 A. A. Zadorozhnaya and A. I. Krylov, "Zooming into π -stacked manifolds of nucleobases: Ionized states of dimethylated uracil dimers," J. Phys. Chem. A 114, 2001 (2010).
- 3 K. B. Bravaya, O. Kostko, M. Ahmed, and A. I. Krylov, "The effect of π -stacking, H-bonding, and electrostatic interactions on the ionization energies of nucleic acid bases: Adenine-adenine, thymine-thymine and adenine-thymine dimers," Phys. Chem. Chem. Phys. 12, 2292 (2010).
- 4 P. Nijjar, A. I. Krylov, O. V. Prezhdo, A. F. Vilesov, and C. Wittig, "Conversion of He(2^3 3S) to He₂($a^3\Sigma^+$) in liquid helium," J. Phys. Chem. Lett. **9**, 6017 (2018).
- ⁵P. Nijjar, A. I. Krylov, O. V. Prezhdo, A. F. Vilesov, and C. Wittig, "Triplet excitons in small helium clusters," J. Phys. Chem. A **123**, 6113 (2019).
- ⁶K, Diri and A. I. Krylov, "Electronic states of the benzene dimer: A simple case of complexity," J. Phys. Chem. A 116, 653 (2011).
- ⁷E. S. S. Iyer, A. Sadybekov, O. Lioubashevski, A. I. Krylov, and S. Ruhman, "Rewriting the story of excimer formation in liquid benzene," J. Phys. Chem. A 121, 1962 (2017).
- ⁸L. Rayleigh, "Series of emission and absorption bands in the mercury spectrum," Proc. R. Soc. A 116, 702 (1927).
- ⁹J. J. Hopfield, "Absorption and emission spectra in the region $\lambda = 600-1100$," Phys. Rev. 35, 1133 (1930).
- $^{10} \rm J$. J. Hopfield, "New ultra-violet spectrum of helium," Astrophys. J. 72, 133 (1930).
- ¹¹T. H. Förster and K. Kasper, "Ein Konzentrationsumschlag der Fluoreszenz," Z. Phys. Chem. (NF) 1, 275 (1954).
- ¹²J. B. Birks, "Higher excited states of benzene and toluene excimers," Chem. Phys. Lett. 1, 625 (1968).
- ¹³ J. B. Birks, Rep. Prog. Phys. **38**, 903 (1975).
- ¹⁴F. Plasser and H. Lischka, "Electronic excitation and structural relaxation of the adenine dinucleotide in gas phase and solution," Photochem. Photobiol. Sci. 12, 1440 (2013).

- 15 A. Ron and O. Schnepp, "Electronic spectrum of 2,2'-paracyclophane," J. Chem. Phys. 37, 2540 (1962).
- 16 A. Ron and O. Schnepp, "Electronic spectrum of (2, 2)paracyclophane. II," Chem. Phys. 44, 19 (1966).
- ¹⁷A. C. Albrecht, "Olarizations and assignments of transitions: The method of
- photoselection," J. Molec. Spect. **6**, 84 (1961).

 18 O. S. Haggag, N. Levinsky, and S. Ruhman, "Coherent intramolecular excimer formation in solid [2,2]-paracyclophane: Time-resolved springing of a molecular 'trap'" ChemPhotoChem 6, e202200181 (2022).
- ¹⁹A. I. Krylov, "Equation-of-motion coupled-cluster methods for open-shell and electronically excited species: The Hitchhiker's guide to Fock space," Annu. Rev. Phys. Chem. 59, 433 (2008).
- $^{\mathbf{20}}$ J. F. Stanton and R. J. Bartlett, "The equation of motion coupled-cluster method. A systematic biorthogonal approach to molecular excitation energies, transition
- probabilities, and excited state properties," J. Chem. Phys. **98**, 7029 (1993). ²¹ H. Reisler and A. I. Krylov, "Interacting Rydberg and valence states in radicals and molecules: Experimental and theoretical studies," Int. Rev. Phys. Chem. 28, 267 (2009).
- ²²Depending on molecular orientation, symmetry labels corresponding to the same orbital or vibrational mode may be different. Q-Chem's standard molecular orientation is different from that of Mulliken.³⁹ For example, Q-Chem would place water molecule in the xz plane instead of the yz. Consequently, for C_{2v} symmetry, b_1 and b_2 labels are flipped. More details can be found at
- ²³E. Epifanovsky, A. T. B. Gilbert, X. Feng, J. Lee, Y. Mao, N. Mardirossian, P. Pokhilko, A. F. White, M. P. Coons, A. L. Dempwolff, Z. Gan, D. Hait, P. R. Horn, L. D. Jacobson, I. Kaliman, J. Kussmann, A. W. Lange, K. U. Lao, D. S. Levine, J. Liu, S. C. McKenzie, A. F. Morrison, K. D. Nanda, F. Plasser, D. R. Rehn, M. L. Vidal, Z.-Q. You, Y. Zhu, B. Alam, B. J. Albrecht, A. Aldossary, E. Alguire, J. H. Andersen, V. Athavale, D. Barton, K. Begam, A. Behn, N. Bellonzi, Y. A. Bernard, E. J. Berquist, H. G. A. Burton, A. Carreras, K. Carter-Fenk, R. Chakraborty, A. D. Chien, K. D. Closser, V. Cofer-Shabica, S. Dasgupta, M. de Wergifosse, J. Deng, M. Diedenhofen, H. Do, S. Ehlert, P.-T. Fang, S. Fatehi, Q. Feng, T. Friedhoff, J. Gayvert, Q. Ge, G. Gidofalvi, M. Goldey, J. Gomes, C. E. González-Espinoza, S. Gulania, A. O. Gunina, M. W. D. Hanson-Heine, P. H. P. Harbach, A. Hauser, M. F. Herbst, M. Hernández Vera, M. Hodecker, Z. C. Holden, S. Houck, X. Huang, K. Hui, B. C. Huynh, M. Ivanov, Á. Jász, H. Ji, H. Jiang, B. Kaduk, S. Kähler, K. Khistyaev, J. Kim, G. Kis, P. Klunzinger, Z. Koczor-Benda, J. H. Koh, D. Kosenkov, L. Koulias, T. Kowalczyk, C. M. Krauter, K. Kue, A. Kunitsa, T. Kus, I. Ladiánszki, A. Landau, K. V. Lawler, D. Lefrancois, S. Lehtola, R. R. Li, Y.-P. Li, J. Liang, M. Liebenthal, H.-H. Lin, Y.-S. Lin, F. Liu, K.-Y. Liu, M. Loipersberger, A. Luenser, A. Manjanath, P. Manohar, E. Mansoor, S. F. Manzer, S.-P. Mao, A. V. Marenich, T. Markovich, S. Mason, S. A. Maurer, P. F. McLaughlin, M. F. S. J. Menger, J.-M. Mewes, S. A. Mewes, P. Morgante, J. W. Mullinax, K. J. Oosterbaan, G. Paran, A. C. Paul, S. K. Paul, F. Pavošević, Z. Pei, S. Prager, E. I. Proynov, Á. Rák, E. Ramos-Cordoba, B. Rana, A. E. Rask, A. Rettig, R. M. Richard, F. Rob, E. Rossomme, T. Scheele, M. Scheurer, M. Schneider, N. Sergueev, S. M. Sharada, W. Skomorowski, D. W. Small, C. J. Stein, Y.-C. Su, E. J. Sundstrom, Z. Tao, J. Thirman, G. J. Tornai, T. Tsuchimochi, N. M. Tubman, S. P. Veccham, O. Vydrov, J. Wenzel, J. Witte, A. Yamada, K. Yao, S. Yeganeh, S. R. Yost, A. Zech, I. Y. Zhang, X. Zhang, Y. Zhang, D. Zuev, A. Aspuru-Guzik, A. T. Bell, N. A. Besley, K. B. Bravaya, B. R. Brooks, D. Casanova, J.-D. Chai, S. Coriani, C. J. Cramer, G. Cserey, A. E. DePrince, R.

- A. DiStasio, A. Dreuw, B. D. Dunietz, T. R. Furlani, W. A. Goddard, S. Hammes-Schiffer, T. Head-Gordon, W. J. Hehre, C.-P. Hsu, T.-C. Jagau, Y. Jung, A. Klamt, J. Kong, D. S. Lambrecht, W. Liang, N. J. Mayhall, C. W. McCurdy, J. B. Neaton, C. Ochsenfeld, J. A. Parkhill, R. Peverati, V. A. Rassolov, Y. Shao, L. V. Slipchenko, T. Stauch, R. P. Steele, I. E. Subotnik, A. J. W. Thom, A. Tkatchenko, D. G. Truhlar, T. Van Voorhis, T. A. Wesolowski, K. B. Whaley, H. L. Woodcock, P. M. Zimmerman, S. Faraji, P. M. W. Gill, M. Head-Gordon, J. M. Herbert, and A. I. Krylov, "Software for the frontiers of quantum chemistry: An overview of developments in the Q-Chem 5 package," J. Chem. Phys. 155, 084801 (2021).
- ²⁴A. I. Krylov and P. M. W. Gill, "Q-Chem: An engine for innovation," WIREs Comput. Mol. Sci. 3, 317 (2013).
- ²⁵P. Pokhilko, E. Epifanovsky, and A. I. Krylov, "Double precision is not needed for many-body calculations: Emergent conventional wisdom," J. Chem. Theory Comput. 14, 4088 (2018).
- ²⁶ A. V. Luzanov, A. A. Sukhorukov, and V. É. Umanskii, Application of transition density matrix for analysis of excited states, Theor. Exp. Chem. 10, 354 (1976); Russian original:, Teor. Eksp. Khim., 10, 456 (1974).
- ²⁷ A. V. Luzanov and V. F. Pedash, "Interpretation of excited states using chargetransfer numbers," Theor. Exp. Chem. 15, 338 (1980).
- ²⁸F. Plasser, M. Wormit, and A. Dreuw, "New tools for the systematic analysis and visualization of electronic excitations. I. Formalism," J. Chem. Phys. 141, 024106
- ²⁹F. Plasser, S. A. Bäppler, M. Wormit, and A. Dreuw, "New tools for the systematic analysis and visualization of electronic excitations. II. Applications," J. Chem. Phys. 141, 024107 (2014).
- ³⁰A. I. Krylov, "From orbitals to observables and back," J. Chem. Phys. 153, 080901 (2020).
- ³¹S. A. Mewes, F. Plasser, A. Krylov, and A. Dreuw, "Benchmarking excitedstate calculations using exciton properties," J. Chem. Theory Comput. 14, 710
- $^{\bf 32}$ F. Plasser and H. Lischka, "Analysis of excitonic and charge transfer interactions from quantum chemical calculations," J. Chem. Theory Comput. 8, 2777 (2012).
- ³³F. Plasser, A. I. Krylov, and A. Dreuw, "libwfa: Wavefunction analysis tools for excited and open-shell electronic states," WIREs Comput. Mol. Sci. 12, e1595 (2022)
- ³⁴S. Gozem and A. I. Krylov, "The ezspectra suite: An easy-to-use toolkit for spectroscopy modeling," WIREs Comput. Mol. Sci. 12, e1546 (2022).
- ³⁵W. Li, Z. Sui, H. Liu, Z. Zhang, and H. Liu, "High-pressure Raman study of [2,2]-paracyclophane," J. Phys. Chem. C 118, 16028-16034 (2014).
- ³⁶W. Goldacker, D. Schweitzer, K. P. Dinse, and K. H. Hausser, "Influence of an identified dimer vibration on the emission spectrum of [2,2]-paracyclophane. Chem. Phys. 48, 105 (1980).
- ³⁷H. Wolf, D. Leusser, M. Jørgensen, R. Herbst-Irmer, Y.-S. Chen, E.-W. Scheidt, W. Scherer, B. B. Iversen, and D. Stalke, "Phase transition of [2,2]paracyclophane—An end to an apparently endless story," Chem. - Eur. J. 20, 7048
- ³⁸M. O. Sinnokrot and C. D. Sherrill, "Highly accurate coupled cluster potential energy curves for the benzene dimer: Sandwich, T-shaped, and parallel-displaced configurations," J. Phys. Chem. A **108**, 10200 (2004). ³⁹ R. S. Mulliken, "Report on notation for the spectra of polyatomic molecules,"
- J. Chem. Phys. 23, 1997 (1955).